ESA Contract No. 4000130930/20/I-DT

TOWARDS THE RETRIEVAL OF LAKE ICE THICKNESS FROM SATELLITE ALTIMETRY MISSIONS

(LIAM)

SCIENTIFIC AND TECHNICAL REPORT (TR)

State-of-the-art review, analysis and requirement review

Issue / Revision: 1 / 2

Date: 18.12.2020

Prepared by

Claude Duguay, H2O Geomatics Inc.

Ghislain Picard, Institut des Géosciences de l'Environnement-Université Grenoble Alpes

Elena Zakharova, Ocean Next (now with EOLA Micro-Enterprise)

APPROVAL

Signature		
Date	07.10.2020	21.12.2020
Surname	C. Duguay	J. Benveniste
Affiliation	H2O Geomatics	ESA

ESA STUDY CONTRACT REPORT

ESA CONTRACT NO.	SUBJECT:	CONTRACTOR:
4000130930/20/I-DT	LIAM – SCIENTIFIC AND TECHNICAL REPORT (TR)	H2O Geomatics Inc.

ABSTRACT:

This document provides a review of radiative transfer models relevant for investigating the sensitivity of microwave signals to ice properties and state-of-the-art methods for the retrieval of lake ice cover/open water and ice thickness from space-based active and passive microwave operating at frequencies relevant to altimeter missions (i.e. 5-37 GHz). The review is followed by a description of the lakes selected for the study and available data sets from altimeter missions and secondary sources (i.e. in situ measurements, ice charts and other satellite products), as well as the microwave radiative transfer and the thermodynamic lake ice models to be used. Experiments to be conducted with the models and planned comparisons between forward simulations of backscatter/brightness temperature and measurements from altimeter missions are then summarized.

The work described in this report was done under ESA Contract. Responsibility for the contents resides in the author or organisation that prepared it.

AUTHORS: Claude Duguay, Ghislain Picard and Elena Zakharova

ESA Study Manager: Jérôme Benveniste	ESA BUDGET HEADING

DOCUMENT CHANGE LOG

Issue/ Revision	Date	Modification	Modified pages	Comment

Table of Contents

1. INTRODUCTION

1.1. Purpose of the document

This document provides a state-of-the-art review of radiative transfer models relevant for investigating the sensitivity of microwave signals to ice properties and methods for the retrieval of lake ice cover/open water and ice thickness from space-based active and passive microwave operating at frequencies relevant to altimeter missions (i.e. 5-37 GHz). It also contains a description of the datasets and models to be used, and a summary of sensitivity experiments and comparison with measurements from altimeter missions to be conducted leading to the midterm report and the final report.

1.2. Structure of the document

This document contains four main sections in addition to the Introduction and list of references. Section 2 provides a comprehensive review of microwave radiative transfer models previously used in lake ice studies and remote sensing of lake ice. Section 3 contains a description of the lakes selected as well as data from altimeter missions and secondary sources (i.e. in situ measurements, ice charts and other satellite products) available for the study. Section 4 provides a description of the snow microwave radiative transfer (SMRT) model, which now includes a representation of freshwater lake ice, and the thermodynamic lake ice model to be used during the course of the project. Experiments to be conducted with the two models and planned comparison between SMRT output (i.e. forward simulations of backscatter and brightness temperature) and measurements from Jason-2/3 and Sentinel-3 missions are also summarized in this section.

1.3. Applicable documents

- Proposal “Towards the retrieval of lake ice thickness from satellite altimetry missions”, Invitation to Tender AO/1-9101/17/I-NB, EO Science for Society Permanently Open call for proposals (EOEP-5 BLOCK 4).

2. REVIEW OF MICROWAVE RADIATIVE TRANSFER MODELS AND RETRIEVAL ALGORITHMS FOR LAKE ICE

This section contains a brief review of: 1) microwave radiative transfer models that have previously been applied to show the sensitivity of brightness temperature or backscatter to lake ice properties; and 2) approaches to retrieve lake ice cover (extent and phenology) and ice thickness from passive and active microwave data.

2.1. Microwave radiative transfer models in lake ice studies

Field-based (scatterometer), airborne (radiometer) and satellite (scatterometer and imaging SAR) remote sensing measurements supported by in situ observations have been invaluable for documenting the sensitivity of brightness temperature and backscatter to ice thickness, the main variable of interest for retrieval from altimetry missions, and advancing our understanding of scattering mechanisms for snow-free and snow-covered lake ice (e.g. Gunn et al., 2011; Atwood et al., 2015; Gunn et al., 2015a,b; Gunn et al., 2017; Gunn et al., 2018).

Microwave radiative transfer models are a useful complement to remote sensing observations as they allow for examination of the impact of ice parameters with ice growth (e.g. bubble inclusions in congelation ice and snow ice, snow cover characteristics overlaying ice, surface roughness at different interfaces – air-snow, snow-ice and ice-water) on microwave signals through forward simulations which can then be compared to remote sensing measurements of backscatter and brightness temperature (e.g. Gunn et al., 2011; Gunn et al., 2015a).

Here we briefly cover two radiative transfer models that have been used in previous studies on remote sensing of lake ice: the Helsinki University of Technology (HUT) model (Gunn et al., 2011; Kang et al., 2014) and the dense medium radiative transfer under the quasicrystalline approximation (DMRT-QCA) model (Gunn et al., 2015a), with the latter being of most relevance to the radiative transfer model retained in this study and described in section 3.4 (Snow Microwave Radiative Transfer (SMRT) model).

To date, none of the radiative transfer models have been tested, and improved as needed, to examine the sensitivity of backscatter and brightness temperature measurements from altimetry missions to lake ice thickness and other properties of ice (surface and volume contributions).

2.1.1. Helsinki University of Technology (HUT) model

Briefly, the HUT snow emission model is a widely known model originally developed by Pulliainen et al. (1999) to describe the microwave emission of frozen ground covered by a single layer snowpack, characterized by depth, density, snow grain size, temperature and moisture content. It has since been extended to account for a multi-layered snowpack (Lemmetyinen et al., 2010) and freshwater lake ice (Gunn et al., 2011; Kang et al., 2014).

The main characteristics of this model consists of the use of: 1) the delta-Eddington approximation, also called 1-stream approximation, that makes the solution of the radiative transfer equation very simple (Pan et al., 20016); and 2) an empirical representation of the scattering coefficient. As opposed to DMRT (or IBA: Improve Born Approximation) discussed in the next section and for SMRT (section 3.4), HUT scattering is solely based on early experiments on snow scattering and does not have physics-based grounds. The advantage

of the model is a very simple equation for the extinction coefficient (K_e) as a function of the snow "grain-size" *D*.

$$\kappa_e = 0.0018 f^{2.8} D_{obs}^2, \tag{2.1}$$

where *f* is frequency in GHz and *obs* means empirical.

The extension of HUT for passive microwave of lake ice proposed in Gunn et al. (2011) and in Kang et al. (2014) adds support for an ice layer that is modeled as snow but neglecting scattering. This is thereby valid for pure ice without bubbles.

Another important addition for lake ice studies is the simulation of emissivity at the ice/water interface. The comparison of the simulations with observations had shown that a flat interface – driven by the Fresnel coefficients – was insufficient. Instead, the model for rough soil proposed by Wegmüller and Mätzler (1999) was adopted by replacing soil dielectric constant by that of water. The roughness effect is then taken into account through a semi-empirical height variation parameter called RMS. Validity is expected for small heights relative to the wavelength, that is for a weakly rough surface. In practice the height is fitted, and a value of 1 mm has been found to be a very reasonable value (Gunn et al., 2011; Kang et al., 2014).

2.1.2. Dense medium radiative transfer (DMRT) model

The DMRT model for lake ice was implemented as part of a collaboration between at Institute of Applied Physics—National Research Council (IFAC-CNR) and the University of Waterloo. Detailed results from the application of the model along with ground-based Ku/X-band scatterometer observations are described in Gunn et al. (2015a). A description of the model is provided next along with a summary of the key findings from its application to ice cover on a small shallow lake (less than 3 m) near Churchill, Canada.

2.1.2.1. Description of scattering from lake ice

Scattering from complex layered media is usually described as the sum of surface scattering (which take place at the interfaces between the layers of the medium), the volume scattering which could take place inside of each layer (depending on its composition, if the layer is homogeneous volume scattering does not occur) and the interaction among interfaces and scatterers. Usually, the latter is neglected since its magnitude is some order lower than the volume and surface ones.

2.1.2.2. Surface scattering

Surface scattering takes place at the interface between two media and depends on the dielectric properties of the upper and lower layers as well as on the roughness of the interface. Backscattering at incidence angles used by imaging SAR systems (ca. 20-50 degrees) usually increases with the increase of the roughness and also as the difference between the two permittivities grows. There are several models used to characterize surface scattering. Among the most used is the Small Perturbation Method (SPM, valid for low roughness) (Ulaby et al., 1986), the Geometrical and Physical Optics (GO and PO respectively, valid for high roughness) (Ulaby et al., 1986) and the Advanced Integral Equation Method (AIEM) (Wu and Chen, 2004). The backscattering is expressed by the AIEM as (Brogioni et al., 2010):

$$\sigma^{o}{}_{qp}(k_s,k_i)=\frac{k_1{}^2}{2}e^{-\sigma^2(k_z^2+k_{sz}^2)}\cdot\sum_{n=1}^{\infty}\frac{\sigma^{2n}}{n!}\left|I_{qp}^{n}\right|^2 W^{(n)}(k_{sx}-k_x,k_{sy}-k_y) \tag{2.2}$$

where: *p* and *q* denote the transmitted and received polarization respectively, k_1 is the wavenumber in the upper medium, s is the height standard deviation of the surface roughness, *kx, ky, kz and ksx, ksy, ksz* are the projections along the *x, y* and *z* coordinates of the incident and scattering vectors respectively, I^n_{qp} is given below, and $W^{(n)}$ is the Fourier transform of the nth power of the normalized surface correlation function.

The term I_{qp}^n is

$$\begin{aligned}
I_{qp}^{n} \;=\; & (k_z+k_{sz})^n\; f_{qp}\; e^{-\sigma^2 k_z k_{sz}} \\
& +\frac{1}{4}\Big\{(k_{sz}-q_1)^n\; F_{qp1}^{(+)}\; e^{-\sigma^2(q_1^2-q_1k_{sz}+q_1k_z)} \\
& \quad +(k_{sz}-q_2)^n\; F_{qp2}^{(+)}\; e^{-\sigma^2(q_2^2-q_2k_{sz}+q_2k_z)} \\
& \quad +(k_{sz}+q_1)^n\; F_{qp1}^{(-)}\; e^{-\sigma^2(q_1^2+q_1k_{sz}-q_1k_z)} \\
& \quad +(k_{sz}+q_2)^n\; F_{qp2}^{(-)}\; e^{-\sigma^2(q_2^2+q_2k_{sz}-q_2k_z)}\;\Big\}_{u,v=-k_x,-k_y} \\
& +\frac{1}{4}\Big\{(k_z+q_1)^n\; F_{qp1}^{(+)}\; e^{-\sigma^2(q_1^2-q_1k_{sz}+q_1k_z)} \\
& \quad +(k_z+q_2)^n\; F_{qp2}^{(+)}\; e^{-\sigma^2(q_2^2-q_2k_{sz}+q_2k_z)} \\
& \quad +(k_z-q_1)^n\; F_{qp1}^{(-)}\; e^{-\sigma^2(q_1^2+q_1k_{sz}-q_1k_z)} \\
& \quad +(k_z-q_2)^n\; F_{qp2}^{(-)}\; e^{-\sigma^2(q_2^2+q_2k_{sz}-q_2k_z)}\;\Big\}_{u,v=-k_{sx},-k_{sy}}
\end{aligned} \tag{2.3}$$

where

$$q_m=\sqrt{k_m^2-u^2-v^2}\qquad m=1,2 \tag{2.4}$$

In the previous equation f_{qp} accounts for the Kirchhoff field and $F^{(\pm)}_{qp1,2}$ accounts for the complementary scattered intensities in the upward (+) and downward (-) directions both in the upper and lower medium (the correct expressions of these terms can be found in Brogioni et al. (2010)).

It is worth noting that AIEM is a first order model, thus, along the backscattering direction it is unable to correctly simulate the cross polarizations. Indeed, the cross-pols mathematically vanish in the first order methods. In order to overcome such weakness, a common approach is to use the Oh semi-empirical model (Oh et al., 2002).

2.1.2.3. Volume scattering

Volume scattering occurs inside of the medium, every time that the latter is not homogenous (at the microscale). Examples include snow (air bulk which hosts ice particles) or bubbled ice (ice bulk with air inclusions). In the case of pure ice, there is no volume scattering, the only effect noticeable on the EM signal is the attenuation of the wave while propagating through it. Volume scattering is usually modeled with continuous approaches (homogeneous medium with a fluctuating dielectric constant) or discrete ones (bulk medium which hosts discrete scatterers). The general equation for the radiative transfer is (see Tsang et al., 2007 for details and explanation of terms, also described further below)

$$\cos\theta \frac{d\bar{I}_0(\theta,z)}{dz} = -\overline{\overline{k_e}}\ \bar{I}_0(\theta,z) + \int_0^{\pi/2} d\theta' \sin\theta' [\overline{\overline{P_0}}(\theta,\theta')\bar{I}_0(\theta',z) + \\ + \overline{\overline{P_0}}(\theta,\pi-\theta')\bar{I}_0(\pi-\theta',z)] \quad (2.5)$$

which states that the variation of specific intensity inside the elementary volume is due to the extinction (attenuation plus scattering of the EM waves in all the directions but the observed one) plus the scattering of all the incoming EM waves towards the observed direction. In case of a homogenous loss medium like bubble-free ice, the integral vanishes, and the extinction terms become the attenuation of the wave due to absorption losses. The *P* matrix describes the scattering of the inclusions in the medium (e.g. of the air inclusions in ice) and their distribution. A common approximation is to assume that the scatterers are uniformly distributed inside of the medium and that the scattering follows the Rayleigh approximation or Mie theory (depending on the size of the scatterers with respect to the wavelength) (Tsang et al., 2007). However, this applies only to sparse collections of inclusions, with typical fractional volume less than 1%.

Recently, a multilayer model based on the dense medium radiative transfer theory (DMRT) under the quasi-crystalline approximation (QCA) has been introduced by Tsang et al. (2007). This model was originally developed to account for the scattering of snow in which the ice scatterers are densely packed (typically 30% fractional volume), thus the independent scattering does not apply anymore. DMRT-QCA can account for the scattering of spherical densely packed inclusions inside a host medium. Examples of its performance can be found in Tsang and Kong (2001), and Tsang et al. (2007). However, its formulation is not restricted to model ice sphere hosted in air. Due to the reciprocity theorem, the same model also applies to air inclusions embedded in ice (Dupont et al. 2014). The only strong difference amongst the two cases is in the number and distribution of the scatterers since the inclusions in bubbled ice are less than the ice crystals in snow and thus the medium is less “dense”.

To calculate the backscattering of the snow, the radiative transfer equations have to be solved by imposing the boundary condition at the top and the bottom interfaces of each layer (Tsang and Kong, 2001; Tsang et al., 2007). A brief description of the model is provided below.

For media with a laminar structure, the scattering couples the specific intensity only in two directions: upwards (denoted by $I(\theta,z)$) and specularly downward at the same angle θ (denoted by $I(\pi-\theta,z)$).

The general Vector Radiative Transfer (VRT) equations for each layer can be written as

$$\cos\theta \frac{d\vec{I}(\theta,\phi,z)}{dz} = -\overline{\overline{k_e}}(\theta,\phi)\,\vec{I}(\theta,\phi,z) + \int_0^{\pi/2} d\theta' \sin\theta' \int_0^{2\pi} d\phi' [\overline{\overline{P}}(\theta,\phi;\theta',\phi')\,\vec{I}(\theta',\phi',z) + \overline{\overline{P}}(\theta,\phi;\pi-\theta',\phi')\,\vec{I}(\pi-\theta',\phi',z)] \quad (2.6)$$

$$-\cos\theta \frac{d\vec{I}(\pi-\theta,\phi,z)}{dz} = -\overline{\overline{k_e}}(\pi-\theta,\phi)\,\vec{I}(\pi-\theta,\phi,z) + \int_0^{\pi/2} d\theta' \sin\theta' \int_0^{2\pi} d\phi' [\overline{\overline{P}}(\pi-\theta,\phi;\theta',\phi')\,\vec{I}(\theta',\phi',z) + \overline{\overline{P}}(\pi-\theta,\phi;\pi-\theta',\phi')\,\vec{I}(\pi-\theta',\phi',z)] \quad (2.7)$$

where $\bar{I}(\theta,\phi,z)$ is the specific intensity, k_e is the extinction coefficient, P is the phase matrix of the discrete random medium. The first equation stands for the upward intensity and the latter is for the downward one. The procedure to compute k_e and P can be found in Tsang and Kong (2001). Thus, for a n-layer medium, the model yields $2n$ equations.

To solve the radiative transfer problem, $2n$ boundary conditions must be imposed. They are:

$$\vec{I}_1(\pi-\theta,\phi,z=0) = \overline{\overline{R_{10}}}(\theta)\,\vec{I}_1(\theta,\phi,z=0) + \overline{\overline{T_{01}}}(\theta)\vec{I}_0\;\delta(\cos\theta_0-\cos\theta_{0inc})\delta(\phi_0-\phi_{0inc}) \quad (2.8)$$

$$\vec{I}_j(\pi,\phi,z=-d_j) = \overline{\overline{R_{j,j+1}}}(\theta)\,\vec{I}_j(\pi-\theta\,,\phi\,,z=-d_j) + \overline{\overline{S_{j+1,j}}}(\theta)\,\overline{\overline{T_{j+1,j}}}(\theta)\,\vec{I}_{j+1}(\pi-\theta\,,\phi\,,z=-d_j) \quad (2.9)$$

$$\vec{I}_{j+1}(\pi,\phi,z=-d_j) = \overline{\overline{R_{j+1,j}}}(\theta)\,\vec{I}_{j+1}(\pi-\theta\,,\phi\,,z=-d_j) + \overline{\overline{S_{j,j+1}}}(\theta)\,\overline{\overline{T_{j,j+1}}}(\theta)\,\vec{I}_j(\pi-\theta\,,\phi\,,z=-d_j) \quad (2.10)$$

$$\vec{I}(\pi,\phi,z=-d) = \overline{\overline{R_{ng}}}(\theta)\,\vec{I}_n(\pi-\theta\,,\phi\,,z=-d) \quad (2.11)$$

where θ_0 and θ_{0inc} are angles related by the Snell's law at the upper interface. In $\overline{\overline{R}}(\theta)$ and $\overline{\overline{T}}(\theta)$ are respectively the reflection and transmission coefficients matrices at the interfaces and $\overline{\overline{S}}(\theta)$ are the interpolations matrices which related the specific intensities between adjacent layers.

The radiative transfer problem can be solved by means of the discrete ordinate eigenanalysis technique as described in Tsang and Kong (2001), and Tsang et al. (2007). When all the intensities are computed, the backscattering coefficient can be computed as

$$\sigma_{\beta\alpha}(\theta_{0inc}) = 4\pi \frac{\cos\theta_{0inc}\; I_{0\beta}^{(D)}(\theta_{0inc},\phi_{inc}+\pi)}{I_{0\alpha}} \quad (2.12)$$

where α and β are the transmitted and received polarizations.

2.1.2.4. Lake-ice backscattering model

In order to assess if backscatter trends measured over lake ice (both as a function of incidence angle and time) can be explained by the volume scattering contribution, an electromagnetic multilayer model based on DMRT-QCA and AIEM is used. A schematic representation of the model is given in Figure 2.1.

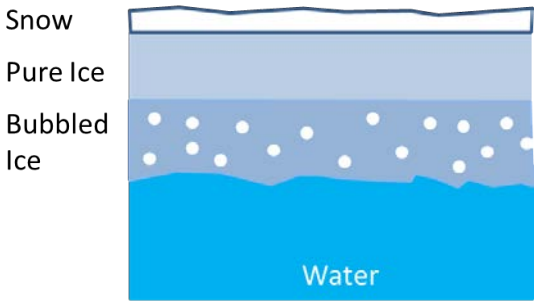

Figure 2.1. Schematic representation of multilayer lake-ice backscattering model based on DMRT-QCA and AIEM.

In this model, there is an upper layer of snow, on top of one layer of pure ice and one of bubbled ice layer above fresh water. In the case where one of the layers is not present (e.g. usually at the beginning of the season when a bubbled ice layer may not exist), the model can be simplified. It is assumed that only the air - snow and the bubbled ice water interfaces have an appreciable roughness, all of the other boundaries were considered flat. The snow layer is simulated by the DMRT under the quasi crystalline approximation, the ice layer without air inclusions is assumed to be pure absorptive, the bubbled ice is simulated also by using DMRT-QCA by inverting host and inclusion media, without stickiness effects. The final expression for the backscattering is

$$\sigma^{TOT}(\theta_i) = \sigma^{S}_{Air-Snow}(\theta_i) + \sigma^{V}_{Ice\ pack}(\theta_i{}') + \sigma^{S}_{Ice\ pack-water}(\theta_i{}')\, e^{-K_{e\ Ice\ pack}\, D_{IP} \sec(\theta_i')} \quad (2.13)$$

where superscripts *TOT*, *S* and *V* refer to total, surface and volume scattering respectively; θ is the incidence angle and the apex refer to the angle refracted in each layer, *D* represents the thickness of the layers, and *IP* ice pack.

2.1.2.5. Model application

The DMRT-QCA model described above treats bubbles as spherical inclusions within an ice volume. Model runs performed by Gunn et al. (2015a) at a shallow lake site (less than 3 m deep) near Churchill, Manitoba (Canada) showed the capability of this model to reproduce observed backscatter magnitude from ground-based Ku/X-band scatterometer systems (ca. 25-70° incidence angles) using snow and ice properties measured in the field as input. The study found that inclusion of spherical bubbles within the ice volume agreed with X-band scatterometer measurements but overestimated those at Ku-band, demonstrating the need for further model modification including the addition of tubular bubbles and roughness considerations at the ice-water interface. Simulations for snow-covered and snow-free ice cover scenarios indicated that the overlying snowpack was a potential source of backscatter at Ku-band and predominantly transparent at X-band, but that other ice properties such surface ice types could confound the snow signal.

2.2. Retrieval of lake ice cover, ice thickness and other ice-related parameters from microwave remote sensing

In this section, we review some of the developments that have taken place in microwave remote sensing of lake ice cover (extent and phenology) and lake ice thickness Other ice parameters believed to introduce uncertainties in retrievals such as bubble inclusions within the ice, snow/ice/water interfaces, and surface deformation features are mentioned where relevant. Focus is placed on the retrieval of these lake ice-related parameters from various passive microwave radiometer and radar (imaging SAR, scatterometer, altimeter) instruments acquiring data at frequencies most relevant to altimeter missions, that is in the range 18-37 GHz (passive microwave) and 5-18 GHz (C- to Ku-band for radar).

2.2.1. Lake ice cover

Lake ice cover is identified as an essential climate variable (ECV) by the Global Climate Observing System (GCOS) (GCOS-200, 2016). The description and units (m^2) provided in GCOS (Table 16, p. 168 in GCOS-200, 2016) suggest that it is synonymous to ice extent/area. GCOS requirements for lake ice cover are 10% (lake-wide) for measurement uncertainty, 1% per decade for temporal stability, 300 m for spatial resolution, and daily temporal resolution.

Microwave remote sensing provides the capabilities for mapping ice cover and open water areas on lakes under cloudy and day/night conditions, which is a significant advantage over optical remote sensing. Investigations on automatic lake ice cover classification algorithms from microwave remote sensing have been limited to date. The algorithms developed have either been traditional classification/segmentation approaches or intensity threshold-based algorithms. The latter are based on the analysis of the temporal evolution of backscatter or brightness temperature, with best results achieved when denser satellite time series are available (daily rather than weekly or monthly acquisitions).

2.2.1.1. Synthetic aperture radar

Threshold-based algorithms - The potential of single and multi-polarized (co-, cross-, and quad-polarization) C-band SAR data has been examined in a few studies to automatically map lake ice cover during the break-up and freeze-up periods. For example, Geldsetzer et al. (2010) analyzed RADARSAT-2 SAR imagery for monitoring ice cover during spring melt on lakes located in the Old Crow Flats, Yukon, Canada. The authors were successful at identifying initial break-up with a simple threshold applied to HH backscatter data (> 81% accuracy) and the main break-up period with a threshold on cross-polarized (HV) data (66%-97%). This method was further developed in Geldsetzer and van der Sanden (2013) for ice classification during the freeze-up period with the determination of thresholds based on polarimetric parameters generated using RADARSAT-2 quad-pol imagery and incidence angle. Similar high accuracies were achieved (76-99%).

The threshold-based method has also used to determine ice phenology. For example, Surdu et al. (2015) used a combination of Advanced Synthetic Aperture Radar (ASAR) and RADARSAT-2 C-band data acquired at VV and HH polarizations to determine ice dates on lakes in northern Alaska. Research conducted on lakes in Central Ontario (Canada) using RADARSAT-2 imagery applied a similar methodology but developed thresholds using the fluctuations in backscatter between different ice phenology stages (i.e. freeze-up to full ice cover and full ice cover to break-up) (Murfitt et al., 2018a). This approach has recently been expanded upon by focusing on the use of the last and largest decrease in backscatter to

identify ice cover phenology for Lake Hazen, Nunavut, Canada from Sentinel-1 C-band data (Murfitt and Duguay, 2020) (Figure 2.2).

Image classification methods - Sobiech and Dierking (2013) evaluated the performance of the unsupervised K-means classification in a binary classification of ice cover and open water on lakes and river channels of the central Lena Delta, northern Siberia. K-means is an unsupervised image classification approach frequently used for mapping river ice types. Using six TerraSAR-X (X-band, single HH co-pol) and three RADARSAT-2 images (C-band, quad-pol HH, VV, HV, and VH simultaneously) obtained during spring 2011, Sobiech and Dierking found that the performance of the K-means classification is comparable to that of a fixed-threshold approach. Application of a low-pass filter prior to the classification of river channels and a closing filter on the classification results of lakes strongly improved the overall k-means classification results. The K-means approach was applied to ca. 1600 C-band SAR (HH and VV-pol) images to analyse variability and short-term trends in ice phenology on 11 lakes of the High Arctic region of Canada over a 15-year period (1997-2011) (Surdu et al., 2016). Segmentation methods for lake ice cover classification have become more sophisticated in recent years. For example, the Iterative Region Growing and Semantics (IRGS) algorithm that was originally developed for the identification of sea ice types has recently been applied to RADARSAT-2 imagery (HH and HV-pol) for the identification of ice cover and open water on Lake Erie (Canada/USA) and Great Bear Lake (Canada), reaching accuracies in the order of 90% (Wang et al., 2018) and 94% (Hoekstra et al., 2020), respectively.

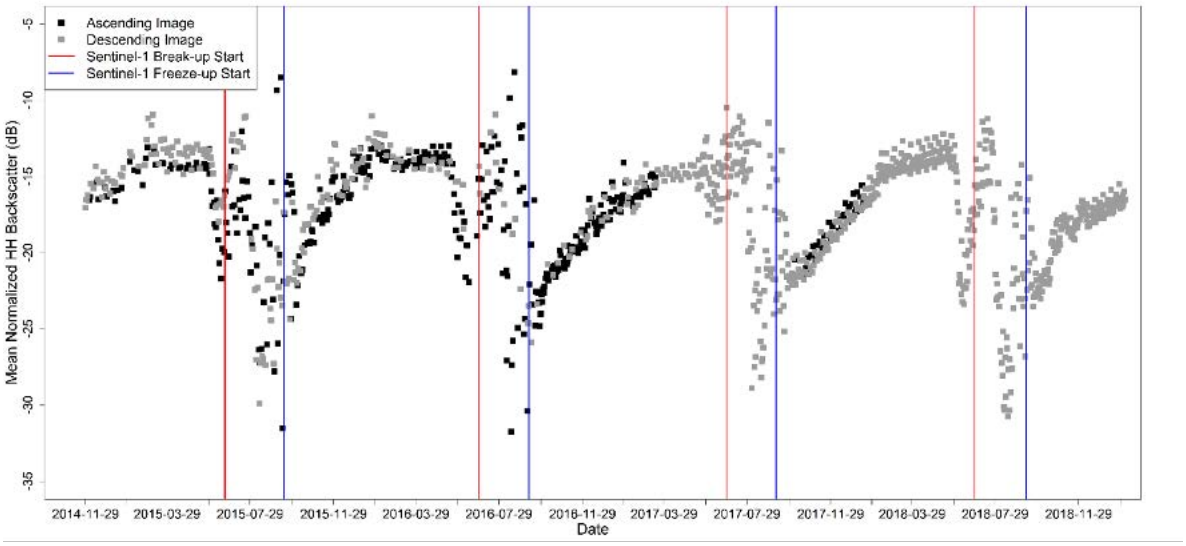

Figure 2.2. Average backscatter evolution of a high-density Sentinel-1 SAR time series for Lake Hazen, Canada (2015–2018). Images acquired at ascending and descending overpasses are represented by black and grey squares, while melt and freeze start times determined from Sentinel-1 images are represented by solid red and blue lines (Source: Murfitt and Duguay, 2020).

2.2.1.2. Scatterometry

Using data from the SeaWinds scatterometer aboard NASA's QuikSCAT satellite (operational from June 1999 until November 2009), Howell et al. (2009) developed an algorithm to map the spatial distribution dates associated with ice phenology on Great Bear Lake (66.02 latitude, -120.61 longitude) and Great Slave Lake (61.58 latitude, -114.20 longitude), Northwest Territories, Canada. Analysis of daily Ku-band (13.4 GHz) backscatter

coefficients σ° (VV, 54.1° incidence angle) from QuikSCAT (4-km enhanced spatial resolution) allows for the detection of melt onset, ice-off and freeze onset (ice-on) dates (Figure 2.3). In winter, σ° exhibits relatively high returns, whereas melt onset is marked by a strong decrease in σ°. Following the first significant downturn in the QuikSCAT σ° temporal evolution, the σ° begins a series of up and downturn oscillations. The first oscillation (i.e. up-turn and down-turn) is related to freeze-thaw processes. The sharp drop in QuikSCAT σ° after this period marks the date when the lake becomes clear of ice (ice-off). The QuikSCAT σ° then increases sharply from the relatively low open-water σ° values to higher σ° values to indicate freeze onset (ice-on). Observed changes in σ° above or below certain threshold values form the basis of the algorithm developed by Howell et al. (2009). Results from the application of the algorithm revealed contrasting patterns in ice phenology parameters within and between the two lakes (2000-2006 period), with ice cover duration lasting five weeks longer on higher latitude lake Great Bear.

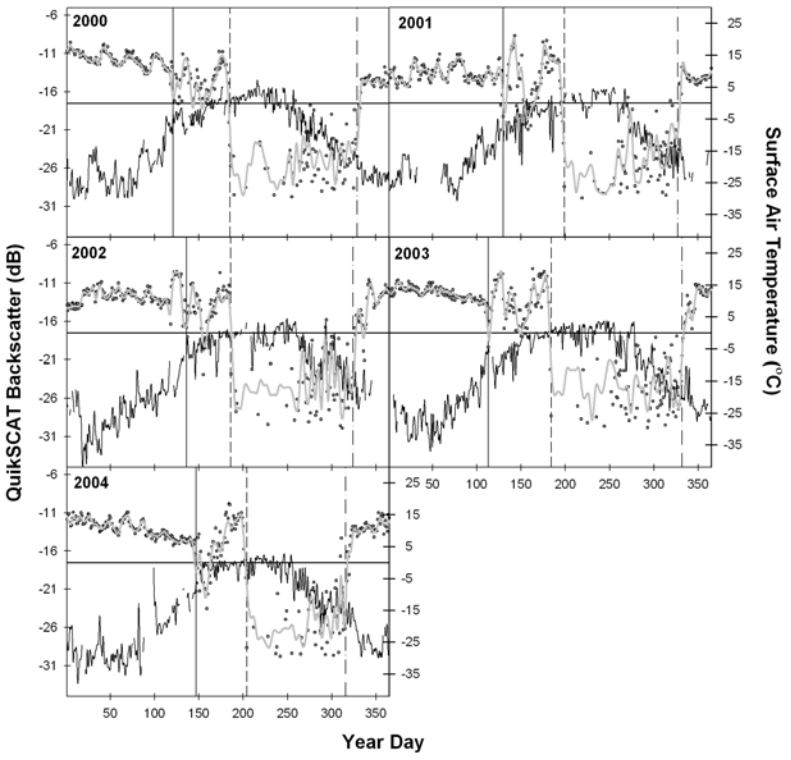

Figure 2.3. Temporal evolution of QuikSCAT Ku-band σ° (left axis) over Great Bear Lake at a test site location from 2000-2004. The first solid vertical gray line represents melt onset, the second vertical dashed grey line represents water clear of ice, the third vertical dashed line represents freeze onset and m, the black time series is APP-x surface air temperature (right axis) (Source: Howell et al., 2009).

2.2.1.3. Passive microwave radiometry

Kang et al. (2012) developed an approach along the same lines as Howell et al. (2009) described above but instead using daily time series of brightness temperature measurements from the Advanced Microwave Scanning Radiometer–Earth Observing System (AMSR-E; fixed incident angle of 54.8°). Brightness temperature of open water is lower than that of ice, more so at H-pol. The study suggested the use of the 18.7 GHz H-pol channel for the detection of ice phonological events (freeze-onset/melt-onset and ice-on/ice-

off dates as well as ice cover duration) on Great Bear Lake (GBL) and Great Slave Lake (GSL), although, as shown in Figure 2.4, the 23.8 and 36.5 GHz channels (H-pol in particular) also show some potential. More recent work by Du et al. (2017) further demonstrates that automated lake ice retrievals is possible from AMSR-E/AMSR-2 36.5 GHz channel (H-pol) over the Northern Hemisphere with daily temporal fidelity and 5-km gridding based on the application of a moving t-test algorithm. Indeed, the authors successfully applied the algorithm to analyze short-term trends (2002-2015) in ice-on/ice-off dates and ice cover duration on the largest lakes (n=71) of the Northern Hemisphere.

The work summarized above clearly demonstrates the value of brightness temperature measurements obtained at frequencies utilized aboard passive microwave radiometer and also nadir-pointing altimeter missions (ca. 18-37 GHz) for discriminating open water from ice-covered areas. Better discrimination is achieved using higher density time series (e.g. daily vs 10-day acquisitions).

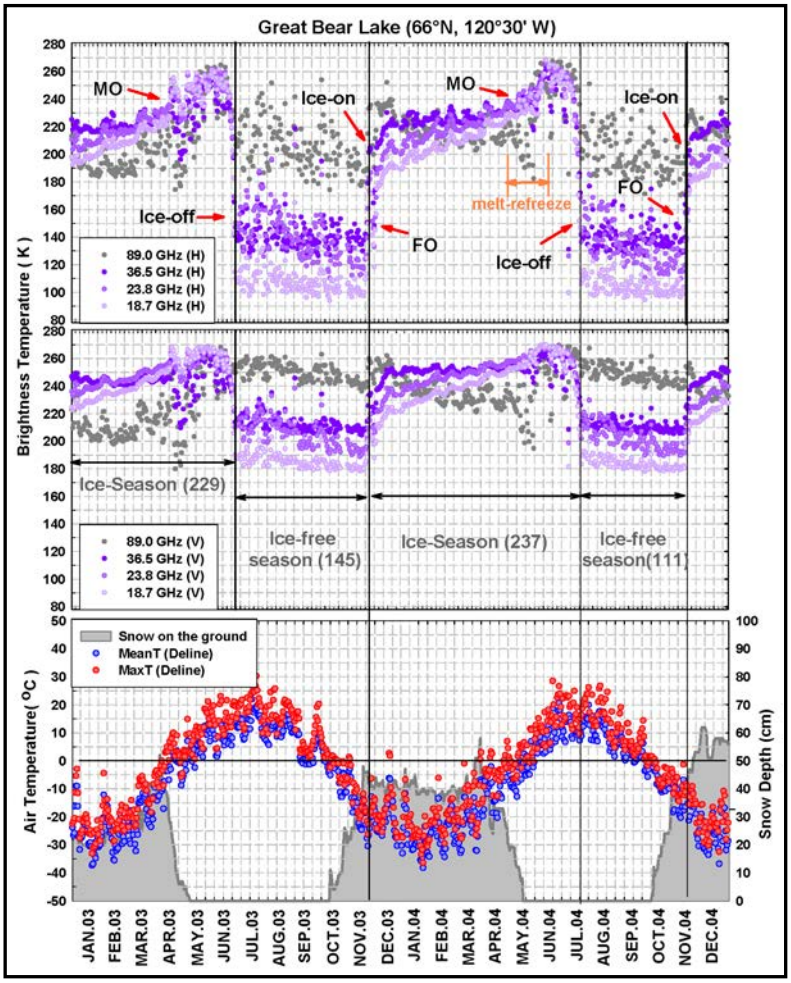

Figure 2.4. Temporal evolution of horizontal (top) and vertical (middle) polarized brightness temperature at 18.7 (light violet), 23.8 (middle violet), 36.5 (dark violet), 89.0 (dark grey) GHz (2003 – 2004) for sampling site on Great Bear Lake, Canada. FO is freeze-onset and MO is melt-onset. The time series of maximum (Max_T, red) and mean (Mean_T, blue) air temperatures obtained at Deline meteorological station is shown in the bottom panel of the figure, with snow depth as grey shaded area. Numbers after both “Ice Season” and “Ice-free Season” indicate number of days (Source: Kang et al., 2012).

2.2.1.4. Radar altimetry and radiometry synergy

A methodology for ice discrimination has been developed and tested for the Caspian and Aral seas as well as for the lakes Ladoga, Onega and Baikal (Kouraev et al., 2003, 2007a, 2007b, 2008, in press). The approach uses the simultaneous nadir-pointing radar and passive microwave acquisitions available from several altimeter missions (TOPEX/Poseidon, Jason-1, Envisat, GFO, and more) to discriminate ice from open water (Figure 2.5). By analyzing this data, it is possible to define specific dates of ice events (the first appearance of ice, the formation of a stable ice cover, the first appearance of open water and the complete disappearance of ice) along tracks for the water bodies of interest. While the along-track observations do not permit lake-wide determination of ice-covered/open water areas and related dates, they are nonetheless spatially and temporally consistent, and therefore of value for climate studies.

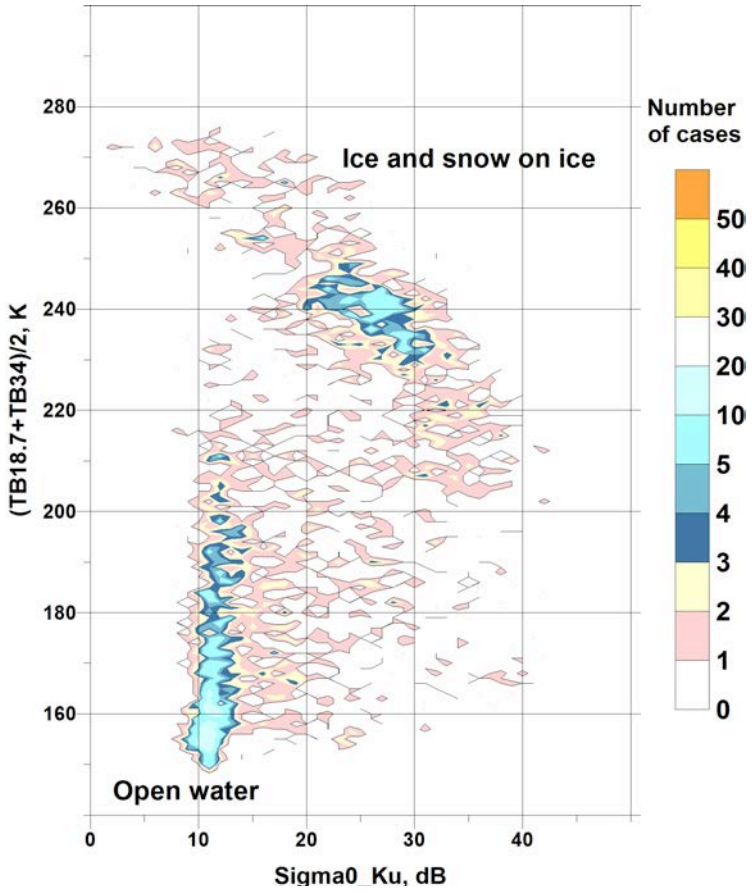

Figure 2.5. Frequency distribution (number of cases; total number of observations (n) = 3,130) of Envisat radar altimeter backscatter observations (Sigma0_Ku in decibel, dB) versus passive (TB18.7+TB34)/2 microwave observations (degrees Kelvin, K) for Cycles 11 to 30 (5 November 2002 to 4 October 2004) over Lake Baikal, Russia. Two well-defined clusters are easily identifiable making it possible to discriminate open water from ice cover (Source: Duguay et al., 2015).

The detection of ice cover and open water areas along tracks is an important step as part of the development of processing chains for the retrieval of lake ice thickness from altimetry missions. Only when footprints along tracks are determined to be ice covered (without melt occurrence) should a thickness retrieval be performed.

2.2.2. Lake ice thickness

Lake ice thickness is identified as an ECV by GCOS (GCOS, 2016). GCOS requirements for lake ice thickness are 1-2 cm for measurement uncertainty, N/A for temporal stability, 100 m for spatial resolution, and monthly temporal resolution. It should be noted that these requirements apply to both in-situ and satellite-based measurements. It is expected that a measurement uncertainty in the order of 10-15 cm may be achievable from altimetry missions (Duguay et al., in prep.).

2.2.2.1. Synthetic aperture radar

Ice thickness is a difficult parameter to estimate from SAR data. It has been shown that increases in backscatter during the ice growth season (see Figure 2.2 for example) is predominantly caused by changes in roughness at the ice-water interface rather than ice thickness. Recent research has evaluated the relation between ice thickness and RADARSAT-2 C-band backscatter for a lake located in Central Ontario, Canada (Murfitt et al., 2018b), but found that retrieval errors were large above 40 cm ice thicknesses. This may be due to a steeper increase in roughness associated with early ice growth as demonstrated in other analysis of polarimetric decomposition experiments for a lake in Churchill, Manitoba, Canada (Gunn et al., 2018).

2.2.2.2. Scatterometry

Ground-based radar experiments data have shown success at estimating ice thickness. The most promising method on local scales has been the application of Frequency Modulated Continuous Wave (FMCW) radars. A method was explored using a X and Ku-band (9.6 and 17.2 GHz) scatterometer system deployed on lake ice near Churchill, Manitoba (Gunn et al., 2015b). This research showed that the analysis of waveforms – the distance of peak returns from the ice-surface to ice-bottom interface for X and Ku-band frequencies – can be used to estimate thickness with R^2 (RMSE) values of 0.953 (0.053 m) and 0.964 (0.088 m) at X and Ku-band, respectively (Figure 2.6) (Gunn et al., 2015b). This study concluded that further work is needed to investigate the impact of various snow and freshwater ice properties on backscatter (e.g. presence bubbled freshwater ice).

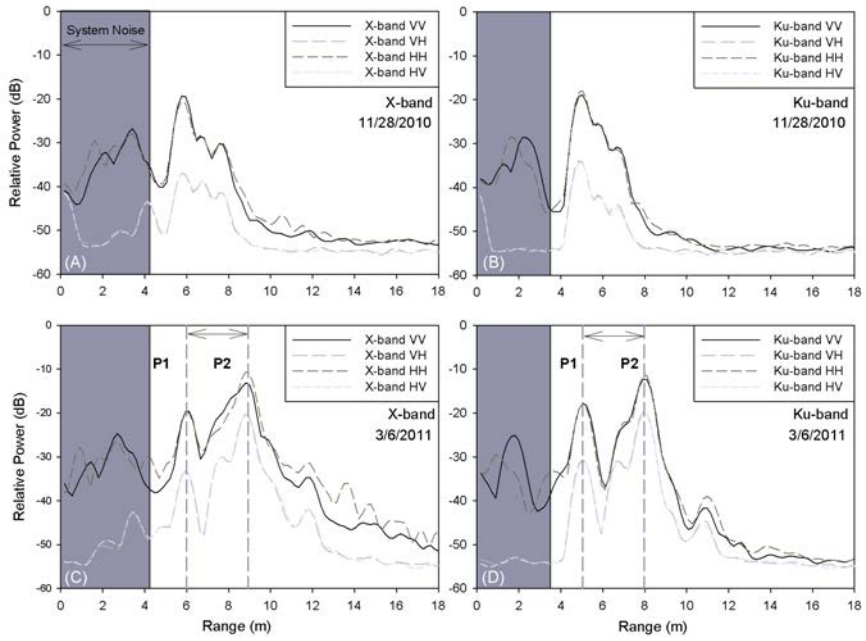

Figure 2.6. Fitted range profiles for X- (A, C) and Ku-bands (B, D) representing an early (A, B) and late season (C, D) observation. The second peak in C and D was not present in early season observations (A, B) due to thin ice (0.4 m). The distance between the two peaks (P2 – P1) was considered to be the distance the signal traveled within the ice volume. (Source: Gunn et al., 2015b).

2.2.2.3. Passive microwave radiometry

Kang et al. (2010) have shown that the temporal evolution of brightness temperature measurements from the AMSR-E 10.7 GHz and 18.7 GHz frequency channels during the ice growth season on Great Bear Lake (GBL) and Great Slave Lake (GSL), Canada, is strongly correlated with ice thickness as estimated with the numerical lake ice model CLIMo (Duguay et al., 2003). Using AMSR-E data from 2002-2007, the authors showed that over 90% of the variations in brightness temperature on GBL and GSL could be explained by the seasonal evolution of ice thickness on these lakes in winter. The strong relation between brightness temperature (TB) at 18.7 GHz V-pol and ice growth from the lake ice model was then explored by Kang et al. (2014) for the development of regression-based ice thickness (ICT) retrieval algorithms. Simple linear regression equations (ICT_{GBL} = 3.53 × TB – 737.929 for GBL; ICT_{GSL} = 2.83 × TB – 586.305 for GSL) allow for the estimation of ice thickness (in cm) on a monthly basis from January to April (Figure 2.7) with a mean bias error (MBE) of 6 cm and RMSE of 19 cm.

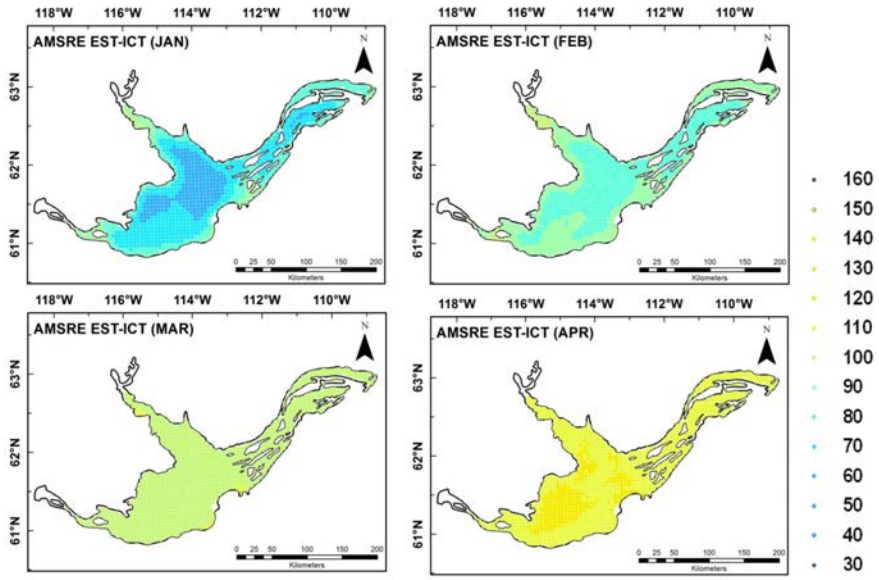

Figure 2.7. Example of ice thickness (in cm) maps for Great Slave Lake (Canada) for the months of January, February, March and April (2002-2009 average) derived from AMSR-E 18.7 GHz V-pol brightness temperature data (Source: Kang et al., 2014).

2.2.2.4. Radar altimetry

Mercier et al. (2011) are the first to have proposed to explore radar altimeter waveforms for the estimation of lake ice thickness via retracking of heights corresponding to

two different peaks on the leading edge. Beckers et al. (2017) evaluated this approach over Great Bear and Great Slave lakes using Cryosat-2 (CS2) waveforms and simple temperature index-based equation to estimate ice thickness. The accuracy of the retrievals was estimated to be in the range of 0.20-0.33 m RMSE (Figure 2.8). However, the validation exercise presented some drawbacks: 1) the suitability of the in situ near-shore ice thickness measurements available compared to those that would otherwise be expected along the CS2 tracks that cover central (deep) sections of the lakes; 2) the use of in situ near-shore field measurements from Great Slave Lake to validate CS2 retrievals at Great Bear Lake, which is known to grow thicker ice than Great Slave (Kang et al., 2014); and 3) the simplicity of the ice growth model used by the authors that ignores the impact of lake depth on the timing of ice formation and, by extension, ice growth/thickness (Duguay et al., 2003). The authors also reported a limited application of the method for thin ice conditions as the minimum waveform peak separation (2 range bins) is approximately 0.26 m in ice.

As in other radar investigations (e.g. Gunn et al., 2015a,b), the study of Beckers et al. (2017) reiterates the fact that ice properties other than thickness likely have an impact on backscatter (power). Clearly, there is a need to investigate the contributions of the various ice and overlying snow properties to backscatter in order to quantify sources of uncertainty in lake ice thickness retrievals from altimetry. The present study will elucidate these contributions through forward simulations with the SMRT model described in section 3.4.

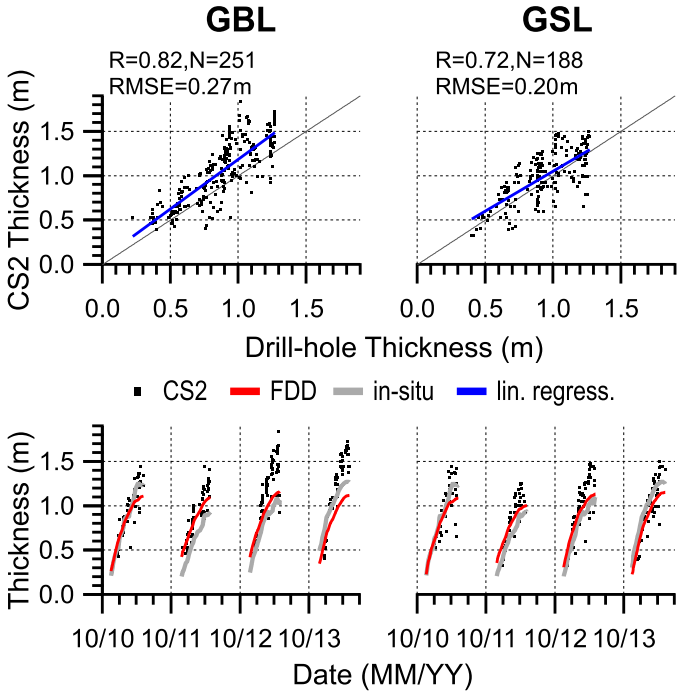

Figure 2.8. Validation results for ice thickness retrievals over GBL and GSL derived from the orbit means of the 10-km along-track averaged CS2 waveforms described in Section V-B. (Top) Scatter plot of CS2 versus in situ ice thickness measurements. The blue line shows the linear regression with slope 1.12±0.05 for GBL and 0.90 ±0.06 for GSL. The black line shows a one-to-one line. (Bottom) Comparison of time series of lake ice thicknesses from CS2, the FDD model, and in situ measurements. (Source: Beckers et al., 2017).

3. DESCRIPTION OF DATA AND MODELS TO BE USED IN STUDY

3.1. Selected lakes

Five lakes are proposed for this study (latitude, longitude): Great Bear Lake (66.02, -120.61), Great Slave Lake (61.58, -114.20), Baker Lake (64.13, -95.28), Lake Superior (47.95, -87.32) and Lake Erie (42.21, -81.25). The lakes were chosen since: 1) they are large, hence covered by one or more Jason-2/3 and Sentinel-3A tracks; 2) they cover a relatively large latitudinal gradient (ca. 66^{o} N to 42^{o} N) that will permit to capture variability in ice conditions influenced by different temperature and snow accumulation regimes; and 3) one or more field-based ice records, ice charts and complementary remote sensing products are available coincident/near-coincident with dates of altimeter acquisitions for each lake, which is necessary for analyzing the impact of ice conditions on backscatter and brightness temperature measurements.

3.2. Data from altimetry missions

The study will analyze radar altimeter and passive microwave radiometer data from three missions: Jason-2, Jason-3 and Sentinel-3A/B. A summary of the time periods for which data is available and the frequencies of acquisitions is provided in Table 3.1.

Emphasis will be placed on the analysis of Jason-2 data since more complete in situ ice records and complementary satellite data products are available for the selected lakes over the period 2008-2016.

Table 3.1. Summary of altimetry missions' data to be used in this study.

Satellite	Period	Altimeter (band/frequency)	Radiometer (frequency)
Jason-2	20 June 2008 – 9 October 2019	Poseidon-3 (Ku/13.6 and C/5.3 GHz)	AMR (18.7, 23.8, 34.0 GHz)
Jason-3	17 January 2016 – present	Poseidon-3B (Ku/13.6 and C/5.3 GHz)	AMR-2 (18.7, 23.8, 34.0 GHz)
Sentinel-3A/B	16 February 2016 – present	SRAL/LRM (Ku/13.6 and C/5.4 GHz)	MWR (23.8 and 36.5 GHz)

3.2.1. Jason-2/3 missions

Data from the Jason-2 and Jason-3 altimetric missions provide a good historical and ongoing coverage with a 10-day repeat orbit which is especially suitable for freshwater ice phenology and thickness monitoring. The Jason altimetric series began in 1992 with the launch of NASA/CNES TOPEX/Poseidon satellite-borne dual-frequency altimeters (centred at 13.6 GHz (Ku-band) and at 5.3 GHz (C-band)) and nadir-looking microwave radiometer (operating at three frequencies: 18, 21, and 37 GHz). In December 2001, the TOPEX/Poseidon was succeeded by the Jason-1 satellite. This was followed by Jason-2 (June 2008) which was launched in the same orbit. Jason-1 provided very few radar altimeter measurements over inland water bodies, especially during the winter period, due to applied sever on-board data filtering procedure (Birkett et al., 2011). This problem was solved for the

Jason-2 mission and, since 2008, many inland water bodies (lakes and rivers) are observed with a 10-day repeat frequency. In July 2017, Jason-2 was manoeuvred into a slightly lower orbit and the Jason-3 satellite, since January 2017, continues to provide altimetry measurements in the same orbit.

Satellites of the Jason series operate in a circular non-sun-synchronous orbit with a 66.03° inclination. Ground track repeatability for Jason-2 and -3 is ±1 km cross-track at the Equator. At higher latitudes, in regions with seasonal ice cover, the repeatability narrows to ± 200-250 m. The radar altimeter provides 20 Hz along-track measurements. The distance between these high-rate measurements at high latitudes is of 370 m. The radar footprint is of 2-12 km, depending on surface roughness. The Advanced Microwave Radiometer (AMR) records are of 1 Hz. For radiometric bands 18.7, 23.8, and 34 GHz the diameter of the footprints is 42, 35, and 22 km, respectively. The main drawback of the Jason satellite series is the low orbit inclination. This fact implies that the observational coverage is limited to lakes located below 66°N in latitude. Nevertheless, this deficiency is compensated by the relatively high temporal (10-day) frequency of observations.

3.2.2. Sentinel-3A/B mission

The European near-polar orbiting satellite Sentinel-3A was launched in February 2016. The orbit inclination is 98.65°, which is optimal for high latitude cryospheric studies. The orbital cycle is 27 days. The sub-monthly monitoring of lakes may be sufficient for the monitoring of ice thickness as required for climate applications. However, this periodicity is less suitable for the determination of ice phenology events (freeze-up, break-up and ice duration) or for operational monitoring of ice thickness. The Sentinel-3A ground track deviation is similar to Jason-2 (±1 km at the Equator). The low periodicity is compensated by higher density of the satellite tracks, which in combination with the analogous satellite Sentinel-3B (placed on the same orbit in April 2018 and moved after 4 months to new intercalated orbit) can significantly improve the frequency ice observation on large lakes.

Sentinel-3A/B are equipped with a new dual-frequency (C-band and Ku-band) Synthetic Aperture Radar Altimeter (SRAL). The SRAL instrument differs from the conventional radar altimeter on Jason-2 and -3. The SAR altimeter is pulse limited across-track (similar to conventional altimeters) and beam limited along-track. The new instrument allows for a significant reduction in measurement noise and higher along-track resolution. The along-track resolution of SAR altimeters is fixed at 320 m (independent from surface roughness) The SRAL measurements are obtained with the same 20 Hz frequency as Jason-2. The Sentinel-3A/B Microwave Radiometer (MWR) is a dual-frequency nadir-looking (23.8 and 36.5 GHz) instrument providing 1Hz measurements of brightness temperature. Since there are no channels operating at the 18-19 GHz range for this mission, the retrieval of ice thickness from radiometry will be limited to thinner ice (likely less than 1 m based on microwave radiative transfer modeling experiments; e.g. Kang et al., 2014).

3.3. Other data sources

3.3.1. In situ ice thickness and on-ice snow depth records

Ice thickness and on-ice snow depth measurements are available for Back Bay on Great Slave Lake (Northwest Territories; 2008-2016) and Baker Lake (Nunavut; 2008-2020) through the Canadian Ice Service (CIS) of Environment and Climate Change Canada (ECCC) (CIS, 2020). These measurements are made at about the same location close to the shore every year on a weekly basis, as soon as the ice cover is safe enough to walk on after freeze-up, and continuing until when the ice becomes unsafe (usually at beginning of break-

up period). Both ice thickness and on-ice snow depth are measured to the nearest centimetre. Since the in situ measurements are made near the shore of lakes, it is expected that they will be only generally representative of conditions encountered further away (several km to tens of km) in the large lakes; at locations where backscatter and brightness temperature data from altimeter missions will be extracted for analysis.

3.3.2. Ice charts

Daily ice charts are available for the Laurentian Great Lakes of North America. For this study, we will extract ice charts of Lake Erie and Lake Superior for a selection of winter dates coincident with those of altimetric acquisitions between 2008 and 2020. The charts are produced by the North American Ice Service (a collaboration between the U.S. National Ice Center and CIS) largely from visual interpretation of the ice conditions from SAR (e.g. RADARSAT-2, Sentinel-1) and optical (e.g. GOES, MODIS) imagery as available by experienced ice analysts. Ice analysts manually draw polygons on imagery, and for each polygon, the ice types, and their estimated concentrations are reported in an oval shape “egg code”. The egg code is the World Meteorological Organization (WMO) standard. Ice charts are color-coded using the international WMO code for total concentration (CT) or stage of development (SD) of ice in the area. Color code CT represents the estimated total ice concentration (in tenths) in each manually drawn polygon. Fast ice that is fastened to the shore is 100 percent concentration by definition. Color code SD is the ice type that has highest partial concentration in that polygon. The color code for CT is used when concentration is more variable than stage of development, while the color code for SD is intended to be used when stage of development is more variable than concentration (Wang et al., 2018).

An example CT and SD ice charts for the western Great Lakes produced for 5 March 2015 is presented in Figure 3.1. Table 3.2 describes SD classes with their corresponding ice thickness ranges and ice-type codes (CIS, 2005). The charts will provide useful information for examination of the impact of ice conditions on backscatter and brightness temperature values extracted along altimeter tracks.

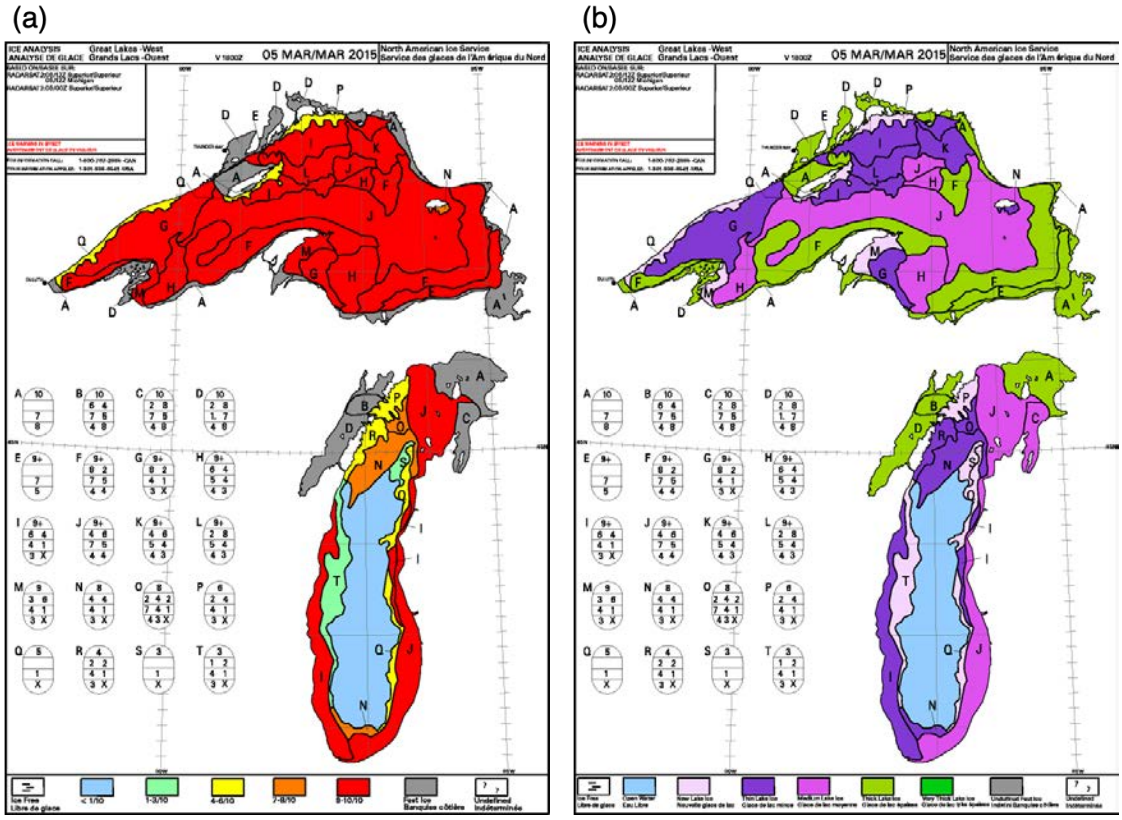

Figure 3.1. Example of ice charts for the western part of the Laurentian Great Lakes (Lake Superior and Lake Michigan) on 5 March 2015 with (a) WMO total concentration (CT) color code (b) WMO stage of development (SD) color code. For each egg, the first line corresponds to total ice concentration, the second line to partial concentration, the third line to stage of development and last line form of ice. For example, in the case of egg A, total concentration is 10 tenth, no partial concentration, stage of development is 7 (30-70 cm ice thickness), and form of ice is 8 (fast ice).

Table 3.2. Description of lake-ice stages of development (CIS, 2005).

Stage of Development	Thickness (cm)	Ice-Type Code
New lake ice	< 5	1
Thin lake ice	5–15	4
Medium lake ice	15–30	5
Thick lake ice	30–70	7
Very thick lake ice	> 70	1 •

3.3.3. RADARSAT-2, Sentinel-1 and MODIS images

SAR (RADARSAT-2/Sentinel-1A) and MODIS satellite images available coincident or near-coincident altimeter missions' acquisitions will permit to examine the effect of variable ice types and ice surface features (e.g. rafted ice, ridged ice, hummocked ice) on radiometric

and altimetric signals, including waveforms. Variable ice types and surface features could introduce uncertainty in the retrieval of ice thickness, hence the magnitude of their impact on backscatter and brightness temperature measurements should be documented.

Over 800 RADARSAT-2 and Sentinel-1A (HH and VV polarizations) images, and as many MODIS images have been collected that cover the selected lakes for the 2008-2016 period. A sample of images for each of the five lakes will be selected in support of the analysis of altimeter missions' signals with an emphasis on Jason-2, given the better data overlap with other satellite products during that period.

3.4. Snow Microwave Radiative Transfer (SMRT) model

The Snow Microwave Radiative Transfer (SMRT) model was initially developed through an ESA ITT (2015-2017) to study the spectral signature of the microstructure of snow (Picard et al., 2018; also see SMRT Homepage at https://www.smrt-model.science/). The objective was to determine how different representations of snow at the micrometer scale impact scattering calculation and, hence, affect passive and active microwave signals as observed by many space-borne sensors.

Snow is a dense medium (e.g. fractional volume of 30% for matured snow) implying that the relative position of the different scatterers (the "snow grains") in the air background has a very strong influence on scattering. For a sparse medium, scattering depends on the scatterers size and shape, and linearly increases as a function of the number of scatterers (called independent scattering) since the scatterers are too far from each other to interact. Typical formulations are given by Rayleigh and Mie scattering theories, when the scatterers are spherical. In a dense medium, the interactions between scatterers become prominent, they usually tend to reduce scattering with respect to the independent scatterer assumption. The size and shape of the scatterers are still important but in the case of snow they become second order with respect to the arrangement between the grains. In the DMRT QCA theory developed by Tsang's group, the grains are assumed spherical (or spheroids) and arrangement with the sticky hard spheres model. This model is controlled by the sphere radius, fractional volume (equivalent to density) and a new parameter the stickiness. This latter parameter is difficult (or impossible) to measure and in practice has become a fitted parameter in most snow studies. The stickiness of snow was found to be very strong (very far from the independent scatterers assumption), but variable. In the Improve Born Approximation (IBA) (Mätzler, 1998), an alternative theory to DMRT-QCA, the scatterers shape, size and arrangement is not explicit, but it is implicitly prescribed by the autocorrelation function (AF) of the ice/air indicator function (Torquato, 2002). This function is not easily measurable and is not intuitive (compared to scatterers shape and size for instance). Mätzler and Wiesman (1999) assumed that the AF takes an exponential form (with some supporting experimental evidences, but that today appears to be too weak) parametrized by a unique parameter (the correlation length). It results that the scattering coefficient depends only on the correlation length and the fractional volume. (where DMRT depends on three parameters). This scattering formulation has been implemented in MEMLS (Mätzler and Wiesman 1999) and is widely used for snow, with many success. While DMRT QCA and IBA have been seen as different (competitive) theories for many years (e.g. Roy et al., 2016), Löwe and Picard (2015) have demonstrated that their electromagnetic grounds were in fact very similar, and that they mostly differ by the snow arrangement model. Hence, by plugging the autocorrelation function corresponding to the sticky hard sphere model into the IBA, IBA and DMRT yield very similar results. This conclusion highlights the critical role of the microstructure in snow and paved the way for SMRT. SMRT was initially developed to cross compare the different theories (e.g. IBA and DMRT QCA) and microstructure representations (SHS, exponential) that were available in different models (MEMLS provided

by Mätzler's group and DMRT-QMS provided by Tsang's group or DMRT-ML provided by Picard's group). SMRT also proposes new microstructure representation. SMRT allows a precision cross comparison because it avoids the noise of the many other implementation details in the existing models that hides the role of the microstructure difference. SMRT was then built with a plugin structure that allows to implement several theories to compute the scattering coefficient and phase function without affecting the remaining of the model. And since this plugin structure appeared to be very efficient, the whole model was in fact implemented in this way.

Despite its relatively narrow initial objective, SMRT has rapidly evolved into a general-purpose radiative transfer model for generic cryospheric environments. In fact, it has been further enhanced in 2018 to represent sea-ice and freshwater lake ice, by adding support to bubbly or saline ice layers as well as fresh and saline water layers. To do so, we reviewed the abundant but scattered literature on this topic, and implemented the different formulations as plugins. It was then possible to represent freshwater lake ice by stacking water, ice, and snow layers overlying a ground substrate. In 2019, in the framework of the CRISTAL mission preparation (ESA ITT PMM), SMRT has been further extended -- in a different direction -- to compute nadir altimetric waveforms by proposing a new method to solve the time-dependent radiative transfer equation (Larue et al., in prep) to the existing discrete ordinate method. The addition of a rough surface was also important for the altimetry and was completed in July 2019 with the implementation of Geometrical Optics and with a partial implementation of the advanced integral equation method (AIEM).

SMRT is now a toolbox proposing numerous pluggable codes at all levels of the microwave radiative transfer calculation. Hence SMRT can technically represent a multilayer stack of snow, ice and water (or even snow, ice, water and ground) and can compute the altimetric waveform (first order backscatter only). However, this has never been performed in practice. Performing good simulations of lake ice requires to: 1) choose the most appropriate theory for the scattering of each component (snow, bubbly ice mainly) and interfaces (air-snow, snow-ice and ice-water interfaces); and 2) set all the required parameters (grain size, microstructure parameters, density, bubble size, roughness, etc.). High level of expert knowledge is needed to adapt the in-situ reality to the best model representation and to compensate for missing information (e.g. roughness, detailed snow microstructure, etc.). Some of the information will be provided by the Canadian Lake Ice Model supported by observations on prevailing ice conditions from in situ ice records, ice charts and complementary remote sensing products described earlier.

3.5. Canadian Lake Ice Model (CLIMo)

The Canadian Lake Ice Model (CLIMo) (Duguay et al., 2003) is a one-dimensional thermodynamic model widely used for freshwater ice cover studies (e.g. Kang et al., 2010; Brown and Duguay, 2011; Kang et al., 2014; Surdu et al., 2014; Gunn et al., 2015; Kheyrollah Pour et al., 2017; Nitze et al., in press) capable of simulating ice on and off dates, thickness and composition of the ice cover (clear or snow ice), temperature profiles within the ice/snow layers on lakes of various depths as well as all components of the radiation and energy balance.

CLIMo is based on the one-dimensional unsteady heat conduction equation, with penetrating solar radiation, where

$$\rho C_p \frac{\partial T}{\partial t} = \frac{\partial}{\partial z} k \frac{\partial T}{\partial z} + F_{sw} I_o (1-\alpha) K e^{-Kz} \tag{3.1}$$

where ρ (kg m^{-3}) is the density, C_p (J kg^{-1} K^{-1}) is the specific heat capacity, T (K) is the temperature, t (s) is the time, k (Wm^{-1}K^{-1}) is the thermal conductivity, z (m) is the vertical coordinate, positive downward, F_{sw} (Wm^{-2}) is the downwelling shortwave radiative energy flux, I_o is the fraction of shortwave radiation flux that penetrates the surface (a fixed value dependent on snow depth), α is the surface albedo, and K is the bulk extinction coefficient for penetrating shortwave radiation (m^{-1}).

The surface energy budget can then be calculated:

$$F_o = F_{lw} - \varepsilon\sigma T^4(0,t) + (1-\alpha)(1-I_0)F_{sw} + F_{lat} + F_{sens} \tag{3.2}$$

where F_o (Wm^{-2}) is the net downward heat flux absorbed at the surface, ε is the surface emissivity, σ is the Stefan–Boltzmann constant (5.67 x 10^{-8} Wm^{-2} K^{-4}), F_{lw} (Wm^{-2}) is the downwelling longwave radiative energy flux, F_{lat} (Wm^{-2}) and F_{sens} (Wm^{-2}) are the latent heat flux and sensible heat flux respectively (both positive downward).

CLIMo includes a fixed-depth mixed layer in order to represent an annual cycle. When ice is present, the mixed layer is fixed at the freezing point and when ice is absent, the mixed layer temperature is computed from the surface energy budget and hence represents a measure of the heat storage in the lake. The water column of shallow lakes is typically well-mixed and isothermal from top to bottom during the ice-free period, permitting the mixed layer depth to be a good approximation of the effect of lake depth leading to autumn freeze-up. In the case of deep lakes, the mixed layer depth is determined either from existing buoy observations or from lake models that predict such depth.

Melt at the upper surface of the ice is determined by the difference between the conductive flux and the net surface flux; the snow (if any) on the ice surface is melted first and the remaining heat is used to melt the ice. The growth and melt of the ice cover at the underside is determined by the difference between the conductive heat flux into the ice and the heat flux out of the upper surface of the mixed layer. The shortwave radiation that penetrates through the bottom of the ice cover is assumed to be absorbed by the mixed layer and returned to the ice underside in order to keep the temperature of the mixed layer at the freezing point. The current version of the model includes a simplified heat exchange between the water column and the lake sediments in the form of a constant heat flux, rather than a varying heat flux that fully captures the annual cycle.

Snow ice is created by the model if there is a sufficient amount of snow to depress the ice surface below the water level. The added mass of the water filled snow pores (slush) is added to the ice thickness as snow ice. The amount of snow ice formed (if any) is not taken into account when melting the ice slab. The albedo parameterization in CLIMo is based mainly on surface type (ice, snow, or open water), surface temperatures (melting versus frozen), and ice thickness, with no distinction regarding ice composition.

CLIMo input forcing data consist of mean daily near-surface air temperature, relative humidity, wind speed, cloud cover and snowfall (or nearby snow depth measurement over land) from which on-ice snow depth is estimated (Figure 3.2). The forcing variables can come from either weather stations located near the lake(s) of interest or atmospheric reanalysis products such as ERA5-land (~9km grid spacing) available from ECMWF. The latter product will provide the forcing variables in this study. Some of the output data from CLIMo will then be fed as input for SMRT forward simulations (ice thickness, snow depth/density, thickness and composition of ice layers, and temperature profiles within the ice/snow layers).

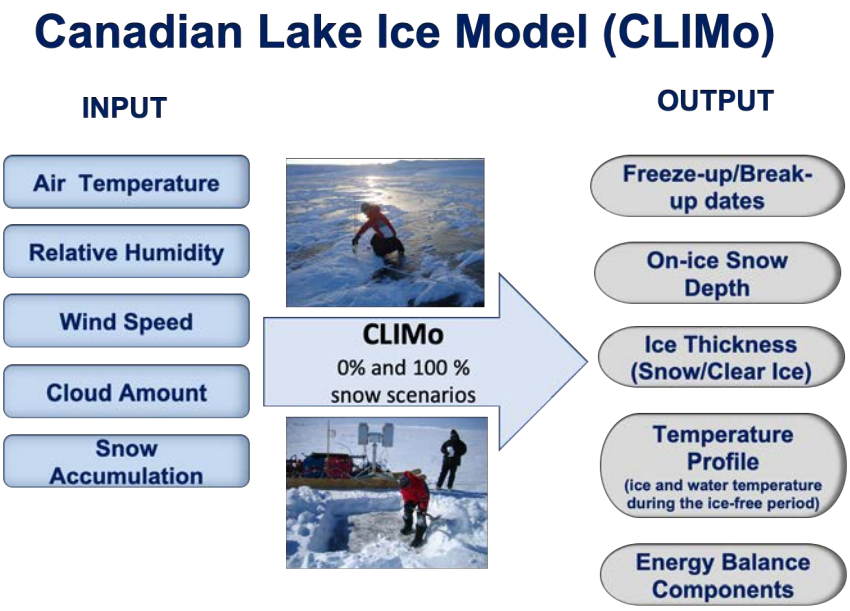

Figure 3.2. Schematic of CLIMo showing input and output variables. The 0% snow scenario corresponds to snow-free conditions on the ice surface and 100% to the same amount that would be measured on land near the lake. The percentage can be varied in simulations to represent the range of possible snow accumulation at different locations on a lake.

4. SUMMARY OF WORK TO BE PERFORMED WITH SELECTED MODELS AND DATA

4.1. Forward modelling of backscatter and brightness temperature using the SMRT model (WP 200)

Combing CLIMo output data (ice thickness, clear ice and snow ice layers, temperature profiles, and on-ice snow depth/density), along with field-based and complementary data (ice charts and satellite products) on prevailing ice conditions for the selected lakes, will provide a physical and geometrical description of the medium that will be fed in SMRT. From that, SMRT can predict backscatter and brightness temperature at any frequency (1-100 GHz), incidence angle and polarization. In addition, it can predict the waveform measured by nadir-viewing altimeters (in LRM mode only) with a newly implemented altimetric module (Larue et al., in prep.). It will therefore be applied to reproduce waveforms from the Jason-2/3 missions (not currently possible in SRAL from Sentinel-3A). In practice, after the first set of simulations, the comparison envisaged under WP 300 will likely show some discrepancies that will need to be resolved by adjusting the most weakly constrained parameters. This is typically the case for surface roughness or the advanced parameters of the microstructure (e.g. stickiness). Work under WP 200 and WP 310 will involve an iterative process. When simulations provide a satisfying agreement with observations, the medium description will be frozen and used in the following.

SMRT will then be used for two main investigations:

1. Understand the microwave-lake ice interactions. For this purpose, SMRT allows to split the contribution of total signal in its different components such as the echoes from the surface, volume (i.e. the layers), interfaces between the layers, the role of the multiple scattering versus direct backscatter, the role of the snow vs ice. Using the altimetric module, it is additionally possible to compute the penetration depth (or the center of gravity in the volume from where the signal is coming on average). For a few studies (a few dates, frequencies, sensors), the mechanism contribution will be computed and analyzed.
2. Explore the sensitivity to noteworthy parameters. Ice thickness is the main variable targeted for both active and passive microwave retrieval, but the signal is sensitive to a wide range of other parameters that will have an impact on the ice thickness retrieval accuracy – introducing some uncertainty. Instances of such variables are: bubble inclusions in congelation ice and snow-ice, snow cover characteristics overlaying ice, surface roughness at different interfaces – air-snow, snow-ice and ice-water. We will explore how the signal changes with changes in these parameters (independently) and will draw conclusions about the potential “noise” introduced by their natural variations. Lastly, the potential to combine frequencies, polarization and active/passive data to maximize the sensitivity to ice thickness (and minimize that of the other parameters) will be assessed using these simulations. This last step should lead to a recommendation on the best configuration to retrieve ice thickness.

Results from this activity will be included in the Mid-Term Review report (MTR).

4.2. Comparison of SMRT model simulations with measurements from altimetry missions (WP 300)

4.2.1. Analysis of altimetry and radiometer data over lakes (WP 310)

A preliminary analysis of Jason-2 and Sentinel-3A radar altimetry measurements over the central basin of Great Slave Lake, Canada, demonstrates a good sensitivity of altimetric instruments to the spatio-temporal variability in ice thickness and texture/roughness. The waveform peak power decreases progressively with ice thickening (Figure 4.1). This reduction is proportional to ice thickness increase (Duguay at al., in prep.; Zakharova et al., in prep.).

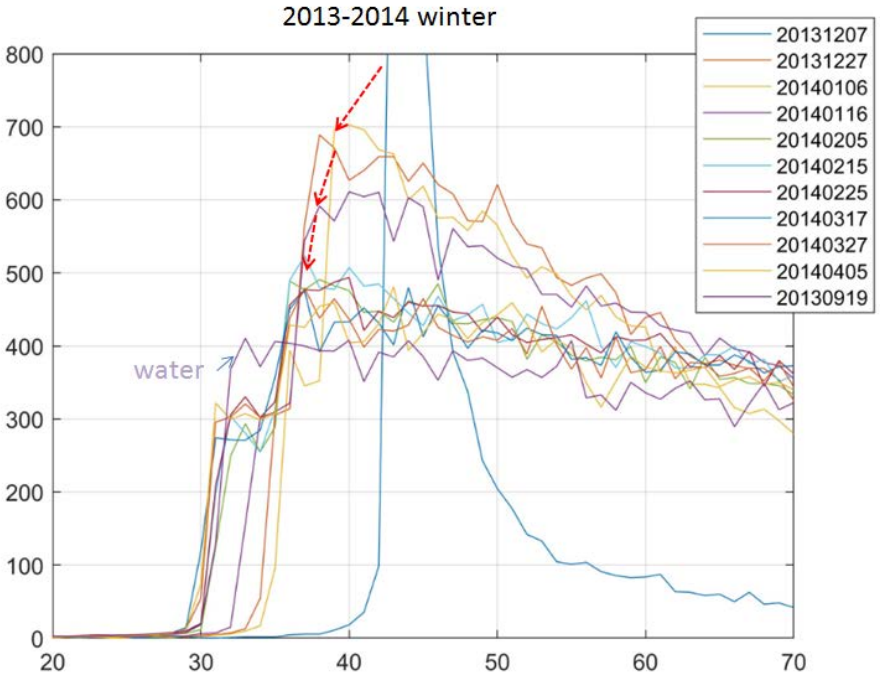

Figure 4.1. Temporal evolution of the Jason-2 waveform during winter 2013-2014 (Great Slave Lake, Canada). The red dashed lines show a progressive decrease in the waveform peak power with ice thickening.

The analysis of altimetric signals allows for the detection of ice floes and deformation features. The latter results in ice ridging and mechanical thickening, as can be seen very clearly on altimetric waveform radiograms as well as in MODIS and RADARSAT-2 SAR images acquired on the same date (Figure 4.2). Both conventional Jason-2 (see Figures 4.1 and 4.2) and Sentinel-3 SAR (Figure 4.3) altimetric signals detect well the main features of the lake ice cover and they evolve in a similar way during ice growth.

Under WP 310, we will conduct an in-depth analysis of along-track variability in backscatter (and waveforms) and brightness temperature measurements with documented variations in ice types and ice surface features provided by other products (ice charts, other satellite data) in a fashion similar to what as shown in Figure 4.2. This analysis will inform forward simulations taking place under WP 200.

Outcomes from WP 310 will be included in the Mid-Term Review report (MTR).

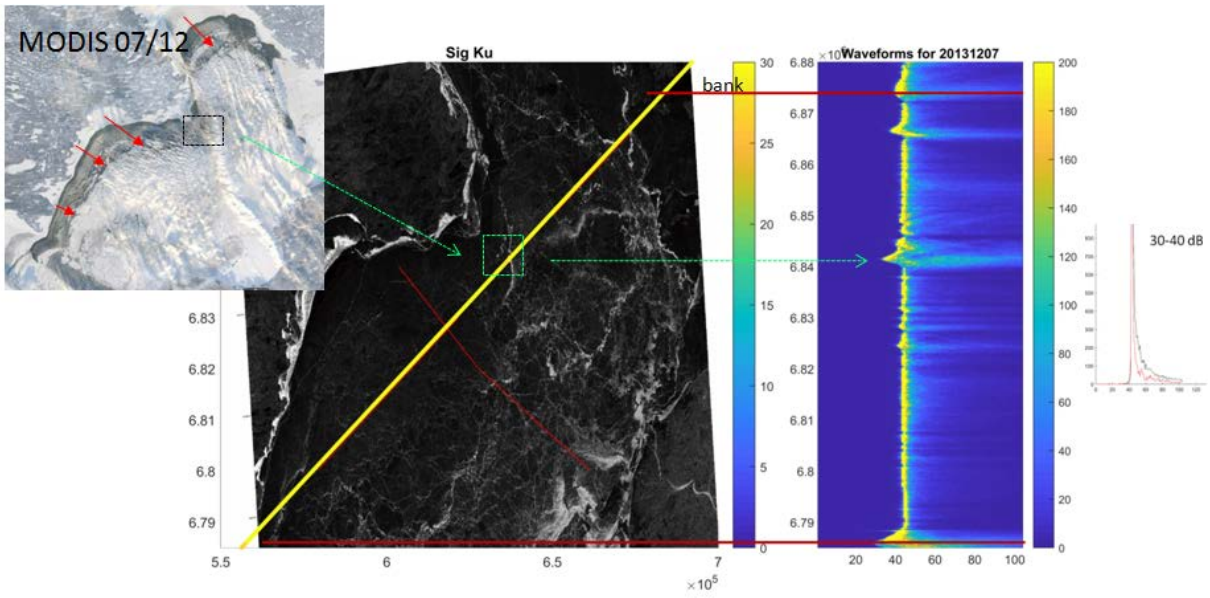

Figure 4.2. Jason-2 along-track waveform variability (Great Slave Lake, Canada) allowing for the detection of a deformation feature (ice ridge; green dashed square) on 7 December 2013 as also seen in MODIS and RADARSAT-2 SAR images.

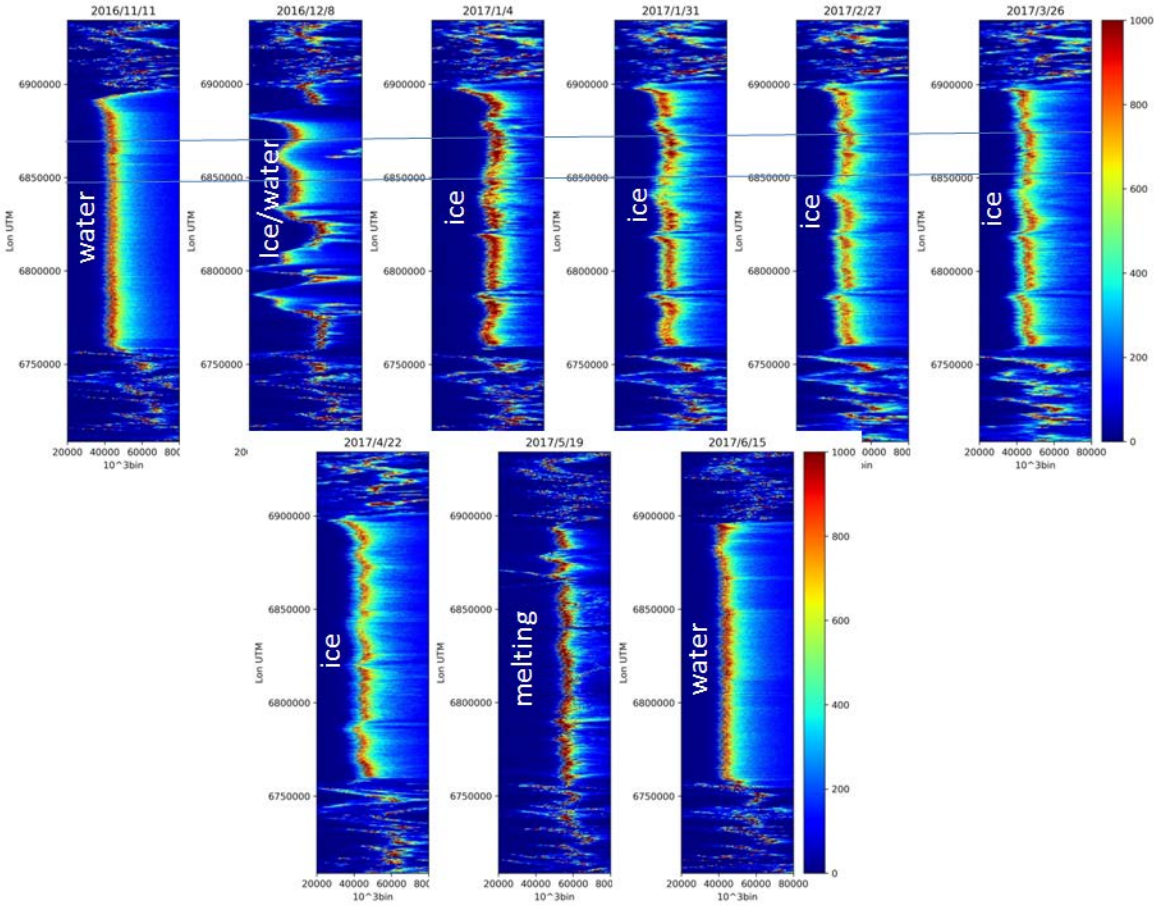

Figure 4.3. Along-track variability of Sentinel-3A waveforms on the Great Slave Lake (Canada) during winter 2016-2017.

4.2.2. Comparison of SMRT simulations with altimetry and radiometer data over lakes (WP 320)

The results of SMRT forward simulations will be compared to a set of independent satellite measurements (i.e. outside of the sample used in the iterative process between WP 200 and WP 310) using general statistics: bias, root mean square error (RMSE) and correlation coefficient for time series of brightness temperature and backscatter. The shape of the waveforms reproduced by SMRT in LRM mode from initial ice formation through to initiation of break-up (i.e. from thinner to thicker ice conditions) will also be compared to that of Jason-2/3. Special attention will be paid to the selection of representative altimetric waveforms from homogeneous to more complex ice conditions (variable ice types and ice surface features). Moreover, the impact of land (banks and islands) on altimetric and radiometric signals over ice cover will be assessed to prevent the selection of inadequate altimetric and radiometric measurements for validation.

Outcomes from WP 320 will be included in the Final Report (FR).

5. REFERENCES

Atwood, D., G. Gunn, C. Roussi, J. Wu, C. Duguay, and K. Sarabandi, 2015. Microwave backscatter from Arctic lake ice and polarimetric implications. *IEEE Transactions on Geoscience and Remote Sensing*, 53(11): 5972-5982, doi: 10.1109/TGRS.2015.2429917.

Birkett C., C. Reynolds, B. Beckley, and B. Doorn, 2011. *From Research to Operations: The USDA Global Reservoir and Lake Monitor, Coastal Altimetry,* Vignudelli et al. (eds.), Springer-Verlag Berlin Heidelberg, DOI: 10.1007/978-3-642-12796-0_2.

Beckers J. F., J.A. Casey, and C. Haas, 2017. Retrievals of lake ice thickness from Great Slave Lake and Great Bear Lake using CryoSat-2. *IEEE Transactions on Geoscience and Remote Sensing*, 55(7): 3708-3720, doi: 10.1109/TGRS.2017.2677583.

Brogioni M., S. Pettinato, G. Macelloni, S. Paloscia, P. Pampaloni, F. Ticconi, and N. Pierdicca, 2010. Sensitivity of bistatic scattering to soil moisture and surface roughness of bare soils. *International Journal of Remote Sensing*, 31: 4227-4255.

Brown, L.C. and C.R. Duguay, 2011. A comparison of simulated and measured lake ice thickness using a Shallow Water Ice Profiler. *Hydrological Processes*, 25: 2932-2941, doi: 10.1002/hyp.8087.

CIS, 2020. Ice thickness data. *Canadian Ice Thickness Program*. https://www.canada.ca/en/environment-climate-change/services/ice-forecasts-observations/latest-conditions/archive-overview/thickness-data.html

CIS, 2005. *MANICE: Manual of standard procedures for observing and reporting ice conditions, 9th ed*. Canadian Ice Service (CIS), Meteorological Service of Canada: Ottawa, ON, Canada, ISBN 0660628589, 146 p.

Du, J., J. S. Kimball, C.R. Duguay, Y. Kim, and J. Watts, 2017. Satellite microwave assessment of Northern Hemisphere lake ice phenology from 2002 to 2015. The Cryosphere, 11: 47–63, doi:10.5194/tc-11-47-2017.

Duguay, C.R., M. Bernier, Y. Gauthier, and A. Kouraev, 2015. Remote sensing of lake and river ice. In *Remote Sensing of the Cryosphere*, Edited by M. Tedesco. Wiley-Blackwell (Oxford, UK), pp. 273-306.

Duguay, C.R., G.M. Flato, M.O. Jeffries, P. Ménard, K. Morris, and W.R. Rouse, 2003. Ice cover variability on shallow lakes at high latitudes: Model simulations and observations. *Hydrological Processes*, 17: 3465-3483.

Duguay, C.R., E.A. Zakharova, A.V. Kouraev, H. Kheyrollah Pour, and J. Murfitt, in prep. Estimation of lake ice thickness from Jason-2 radar altimetry and passive microwave radiometry.

Dupont, F., G. Picard, A. Royer, M. Fily, A. Langlois, A. Roy, and N. Champollion, 2014. Modeling the microwave emission of bubbly ice: Applications to blue ice and superimposed ice in the Antarctic and Arctic. *IEEE Transactions on Geoscience and Remote Sensing,* 52(10), 6639-6651.

GCOS-200, 2016. *The Global Observing System for Climate: Implementation Needs*, 339 p.

Geldsetzer, T. and J.J. van der Sanden, 2013. Identification of polarimetric and nonpolarimetric C-Band SAR parameters for application in the monitoring of lake ice freeze-up. *Canadian Journal of Remote Sensing*, 39: 263-275, https://doi.org/10.5589/m13-033.

Geldsetzer, T., J.J. van der Sanden, and B. Brisco, 2010. Monitoring lake ice during spring melt using RADARSAT-2 SAR. *Canadian Journal of Remote Sensing*, 36: 391-400, https://doi.org/10.5589/m11-001.

Gunn, G., C. Duguay, D. Atwood, J. King, and P. Toose, 2018. Observing scattering mechanisms of bubbled freshwater lake ice using polarimetric RADARSAT-2 (C-band) and UWScat (X-, Ku-band). *IEEE Transactions on Geoscience and Remote Sensing*, 56(5): 2887-2903, doi: 10.1109/TGRS.2017.2786158.

Gunn, G.E., M. Brogioni, C.R. Duguay, G. Macelloni, A. Kasurak, and J. King, 2015a. Observation and modeling of X- and Ku-band backscatter of snow-covered freshwater lake ice. *IEEE Journal of Selected Topics in Applied Earth Observations and Remote Sensing*, 8(7): 3629-3642, doi:10.1109/JSTARS.2015.2420411.

Gunn, G. E., C.R. Duguay, L. Brown, D. Atwood, J. King, and A. Kasurak, 2015b. Freshwater lake ice thickness derived using X- and Ku-band FMCW scatterometers. *Cold Regions Science and Technology*, 120: 115-126, doi: 10.1016/j.coldregions.2015.09.012.

Gunn, G., C. Duguay, C. Derksen, D. Clausi, and P. Toose, 2017. Investigating the influence of variable freshwater ice types on passive and active microwave observations. *Remote Sensing*, 9, 1242, doi:10.3390/rs9121242.

Gunn, G.E., C.R. Duguay, C.P. Derksen, J. Lemmetyinen, and P. Toose, 2011. Evaluation of the Helsinki University of Technology's modified snow emission model over lake ice using airborne passive microwave measurements. *Remote Sensing of Environment*, 115: 233-244, doi:10.1016/j.rse.2010.09.001.

Hoekstra, M., M. Jiang, D.A. Clausi, and C.R. Duguay, 2020. Lake ice-water classification of RADARSAT-2 images by integrating IRGS segmentation with pixel-based random forest labeling. Remote Sensing, 12: 1-21. https://doi.org/10.3390/rs12091425.

Howell, S.E.L., L.C. Brown, K.-K. Kang, and C.R. Duguay, 2009. Variability in ice phenology on Great Bear Lake and Great Slave Lake, Northwest Territories, Canada, from SeaWinds/QuikSCAT: 2000-2006. *Remote Sensing of Environment*, 113: 816–834. https://doi.org/10.1016/j.rse.2008.12.007.

Kang, K.-K., C.R. Duguay, S.E. Howell, C.P. Derksen, and R.E.J. Kelly, 2010. Sensitivity of AMSR-E brightness temperatures to the seasonal evolution of lake ice thickness. *IEEE Geoscience and Remote Sensing Letters*, 7: 751-755, doi: 10.1109/LGRS.2010.2044742.

Kang, K.-K., C.R. Duguay, and S.E. Howell, 2012. Estimating ice phenology on large northern lakes from AMSR-E: Algorithm development and application to Great Bear Lake and Great Slave Lake, Canada. *The Cryosphere*, 6: 235-254, doi:10.5194/tc-6-235-2012.

Kang, K.-K., C.R. Duguay, J. Lemmetyinen, and Y. Gel, 2014. Estimation of ice thickness on large northern lakes from AMSR-E brightness temperature measurements. *Remote Sensing of Environment*, 150: 1-19, http://dx.doi.org/10.1016/j.rse.2014.04.016.

Kheyrollah Pour, H., C.R. Duguay, A. Scott, and K.-K. Kang, 2017. Improvement of lake ice thickness retrieval from MODIS satellite data using a thermodynamic model. *IEEE Transactions on Geoscience and Remote Sensing*, 55(10): 5956-5965, doi: 10.1109/TGRS.2017.2718533.

Kouraev, A.V., F. Papa, P.I. Buharizin, et al., 2003. Ice cover variability in the Caspian and Aral seas from active and passive satellite microwave data. *Polar Research*, 22: 43-50.

Kouraev, A.V., S.V. Semovski, M.N. Shimaraev, N.M. Mognard, B. Legresy, and F. Remy, 2007a. Observations of Lake Baikal ice from satellite altimetry and radiometry. *Remote Sensing of Environment*, 108: 240-253.

Kouraev, A.V., S.V. Semovski, M.N. Shimaraev, N.M. Mognard, B. Legresy, and F. Remy, 2007b. Ice regime of lake Baikal from historical and satellite data: Influence of thermal and dynamic factors. *Limnology and Oceanography*, 52: 1268-1286.

Kouraev, A.V., M.N. Shimaraev, P.I. Buharizin, et al., 2008. Ice and snow cover of continental water bodies from simultaneous radar altimetry and radiometry observations. *Survey in Geophysics*, DOI 10.1007/s10712-008-9042-2.

Kouraev, A.V., J.F. Crétaux, E. Zakharova, et al., in press. Seasonally-frozen lakes in boreal regions. In *Inland Water Altimetry*, Benveniste, J., Vignudelli, S., and Kostianoy, A. (Eds.), Springer.

Larue, F., G. Picard, J. Aublanc, L. Arnaud, A. Robledano-Perez, E. Le Meur, V. Favier, B. Jourdain, J. Savarino, P. Thibaut, in prep. Radar altimeter waveform simulations of the Antarctic ice sheet with the Snow Microwave Radiative Transfer Model (SMRT). To be submitted to *IEEE Transactions on Geoscience and Remote Sensing*.

Lemmetyinen, J., J. Pulliainen, A. Rees, A. Kontu, Y. Qiu, and C. Derksen, 2010. Multiple-layer adaptation of HUT snow emission model: Comparison with experimental data. *IEEE Transactions on Geoscience and Remote Sensing*, 48(7): 2781–2794, doi:10.1109/TGRS.2010.2041357.

Löwe, H. and G. Picard, 2015. Microwave scattering coefficient of snow in MEMLS and DMRT-ML revisited: the relevance of sticky hard spheres and tomography-based estimates of stickiness. *The Cryosphere*, 9: 2101-2117, https://doi.org/10.5194/tc9-2101-2015.

Mätzler, C., 1998. Improved Born approximation for scattering of radiation in a granular medium. *Journal of Applied Physics*, 83(11): 6111–6117.

Mätzler, C. and A. Wiesmann, 1999. Extension of the microwave emission model of layered snowpacks to coarse-grained snow. *Remote Sensing of Environment*, 70(3): 317–325.

Mercier F., J., Tournade, A. Kouraev, O. Gaquiere, and E. Leguay, 2011. Iceberg detection and continental lake ice thickness estimation using altimeter waveforms. *2nd SARAL/ALTIKA Science Workshop*, Ahmedabad, March 15-17.

Murfitt, J., L.C. Brown, and S.E.L. Howell, 2018a. Evaluating RADARSAT-2 for the Monitoring of Lake Ice Phenology Events in Mid-Latitudes. *Remote Sensing*, 10, 1641, https://doi.org/https://doi.org/10.3390/rs10101641.

Murfitt, J., L.C. Brown, and S.E.L. Howell, 2018b. Estimating lake ice thickness in Central Ontario. *PLoS One*, 13, 1–20, https://doi.org/10.1371/journal.pone.0208519.

Murfitt, J. and C.R. Duguay, 2020. Assessing the performance of methods for monitoring ice phenology of the world's largest high arctic lake using high density time series analysis of Sentinel-1 data. *Remote Sensing*, 12, 382; doi:10.3390/rs12030382.

Nitze, I., S. Cooley, C. Duguay, B.M. Jones, and G. Grosse, in press. The catastrophic thermokarst lake drainage events of 2018 in northwestern Alaska: Fast-forward into the future. *The Cryosphere*.

Oh, Y., K. Sarabandi, F.T. Ulaby, 2002. Semi-empirical model of the ensemble averaged differential Mueller matrix for microwave backscattering from bare soil surfaces. *IEEE Transactions on Geoscience and Remote Sensing*, 40: 1348–1355.

Picard, G., M. Sandells, and H. Löwe, 2018. SMRT: An active / passive microwave radiative transfer model for snow with multiple microstructure and scattering formulations (v1.0). *Geoscientific Model Development*, 11: 2763-2788, doi:10.5194/gmd-11-2763-2018.

Pan, J., M. Durand, M. Sandells, J. Lemmetyinen, E. Kim, J. Pulliainen, A. Kontu, and C. Derksen, 2016. Theoretical differences and their effects on the comparison between two snow microwave emission models. *IEEE Transactions on Geoscience and Remote Sensing*, 54(4), doi: 10.1109/TGRS.2015.2493505.

Pulliainen, J.T., J. Grandell, and M.T. Hallikainen, 1999. HUT snow emission model and its applicability to snow water equivalent retrieval. *IEEE Transactions on Geoscience and Remote Sensing*, 37(3): 1378–1390.

Sobiech, J. and W. Dierking, 2013. Observing lake and river-ice decay with SAR: advantages and limitations of the unsupervised K-means classification approach. *Annals of Glaciology*, 54: 65-72. https://doi.org/10.3189/2013AoG62A037.

Surdu, C., C.R. Duguay, L.C. Brown, and D. Fernández Prieto, 2014. Response of ice cover on shallow Arctic lakes of the North Slope of Alaska to contemporary climate conditions (1950-2011): Radar remote sensing and numerical modeling data analysis. *The Cryosphere*, 8: 167-180, doi:10.5194/tc-8-167-2014.

Surdu, C.M., C.R. Duguay, and D. Fernández Prieto, 2016. Evidence of recent changes in the ice regime of lakes in the Canadian High Arctic from spaceborne satellite observations. The Cryosphere, 10: 941-960, https://doi.org/10.5194/tc-10-941-2016.

Surdu, C.M., C.R. Duguay, H. Kheyrollah Pour, and L.C. Brown, 2015. Ice Freeze-Up and Break-Up Detection of Shallow Lakes in Northern Alaska With Spaceborne SAR. *Remote Sensing*, 7, 6133–6159, https://doi.org/10.3390/rs70506133.

Torquato, S., 2002. Random heterogeneous materials: microstructure and macroscopic properties. Springer-Verlag (New York, USA), 703 p.

Tsang, L., J. Pan, D. Liang, Z. Li, D.W. Cline, and Y. Tan, 2007. Modeling active microwave remote sensing of snow using dense media radiative transfer (DMRT) theory with multiple-scattering effects. *IEEE Transactions on Geoscience and Remote Sensing*, 45: 990-1004.

Tsang, L. and J.A. Kong, 2001. *Scattering of electromagnetic waves – Advanced topics*. John Wiley and Sons (New York, USA).

Ulaby, F.T., R.K. Moore, and A.K. Fung, 1986. *Microwave remote sensing: Active and passive*, *Vol. III*, Volume Scattering and Emission Theory, Advanced Systems and Applications, Dedham, Massachusetts, 1797-1848.

Wang, J., C.R. Duguay, and D.A. Clausi, V. Pinard, and S.E.L. Howell, 2018. Semi-automated classification of lake ice cover using dual polarization RADARSAT-2 imagery. *Remote Sensing*, 10(11), 1727; https://doi.org/10.3390/rs10111727.

Wegmüller, U. and C. Mätzler, 1999. Rough bare soil reflectivity model. *IEEE Transactions on Geoscience and Remote Sensing*, 37(3): 1391-1395.

Wu, T.D. and K.S. Chen, 2004. A reappraisal of the validity of the IEM model for backscattering from rough surfaces. *IEEE Transactions on Geoscience and Remote Sensing*, 42: 743-753.

Zakharova, E.A., S. Agaphonova, C.R. Duguay, N. Frolova, and A.V. Kouraev, in prep. River ice phenology and thickness from satellite altimetry.